Icarus 320 (2019) 83–96

Contents lists available at ScienceDirect

Icarus

journal homepage: www.elsevier.com/locate/icarus

# Mineralogy of Occator crater on Ceres and insight into its evolution from the properties of carbonates, phyllosilicates, and chlorides

A. Raponi[a,*], M.C. De Sanctis[a], F.G. Carrozzo[a], M. Ciarniello[a], J.C. Castillo-Rogez[b], E. Ammannito[c], A. Frigeri[a], A. Longobardo[a], E. Palomba[a], F. Tosi[a], F. Zambon[a], C.A. Raymond[b], C.T. Russell[d]

[a] INAF-IAPS Istituto di Astrofisica e Planetologia Spaziali, Via del Fosso del Cavaliere, 100, Rome I-00133, Italy
[b] NASA/Jet Propulsion Laboratory, California Institute of Technology, 4800 Oak Grove Drive, Pasadena, CA 91109, United States
[c] Italian Space Agency (ASI), Via del Politecnico snc, Rome I-00133, Italy
[d] Institute of Geophysics and Planetary Physics, University of California at Los Angeles, 3845 Slichter Hall, 603 Charles E. Young Drive, East, Los Angeles, CA 90095-1567, United States

ARTICLE INFO

*Article history:*
Received 1 August 2017
Revised 24 January 2018
Accepted 2 February 2018
Available online 3 February 2018

ABSTRACT

Occator Crater on dwarf planet Ceres hosts the so-called faculae, several areas with material 5 to 10 times the albedo of the average Ceres surface: Cerealia Facula, the brightest and largest, and several smaller faculae, Vinalia Faculae, located on the crater floor. The mineralogy of the whole crater is analyzed in this work. Spectral analysis is performed from data of the VIR instrument on board the Dawn spacecraft. We analyse spectral parameters of all main absorption bands, photometry, and continuum slope. Because most of the absorption features are located in a spectral range affected by thermal emission, we developed a procedure for thermal removal. Moreover, quantitative modeling of the measured spectra is performed with a radiative transfer model in order to retrieve abundance and grain size of the identified minerals. Unlike the average Ceres surface that contains a dark component, Mg–Ca-carbonate, Mg-phyllosilicates, and $NH_4$-phyllosilicates, the faculae contain mainly Na-carbonate, Al-phyllosilicates, and $NH_4$-chloride. The present work establishes unambiguously the presence of $NH_4$-chloride thanks to the high-spatial resolution data. Vinalia and Cerealia Faculae show significant differences in the concentrations of these minerals, which have been analyzed. Moreover, heterogeneities are also found within Cerealia Facula that might reflect different deposition events of bright material. An interesting contrast in grain size is found between the center (10–60 μm) and the crater floor/peripheral part of the faculae (100–130 μm), pointing to different cooling time of the grains, respectively faster and slower, and thus to different times of emplacement. This implies the faculae formation is more recent than the crater impact event, consistent with other observations reported in this special issue. For some ejecta, we derived larger concentrations of minerals producing the absorption bands, and smaller grains with respect to the surrounding terrain. This may be related to heterogeneities in the material pre-existent to the impact event.



## 1. Introduction

NASA's Dawn spacecraft (Russell and Raymond, 2011) arrived at dwarf planet Ceres on March 6, 2015, with its scientific payload: the Visible and near-InfraRed imaging spectrometer (VIR) (De Sanctis et al., 2011), the Gamma Ray and Neutron Detector (GRaND) (Prettyman et al., 2011), and the Framing Camera (FC) (Sierks et al., 2011), along with radio science (Konopliv et al., 2011).

Ceres' surface shows ubiquitous absorption bands at 2.7 μm (OH stretching) and 3.1 μm related to Mg-phyllosilicates and $NH_4$-phyllosilicates, respectively (De Sanctis et al., 2015; Ammannito et al., 2016). The thermally-corrected spectra of reflectance r (or radiance factor $I/F = \pi r$) of Ceres shows several distinct absorption bands at 3.3–3.5, and 3.95 μm, due to the presence of Mg–Ca carbonates (De Sanctis et al., 2015).

Although the spectral properties of Ceres' surface are quite uniform, there are several peculiar areas with brighter material where significant differences in spectral parameters have been detected, such as slopes, albedo, band depths and band center of specific spectral features (Palomba et al., 2018; Stein et al., 2018). The features that stand out from the surrounding terrains are the bright

* Corresponding author.
*E-mail address:* andrea.raponi@iaps.inaf.it (A. Raponi).

https://doi.org/10.1016/j.icarus.2018.02.001
0019-1035/

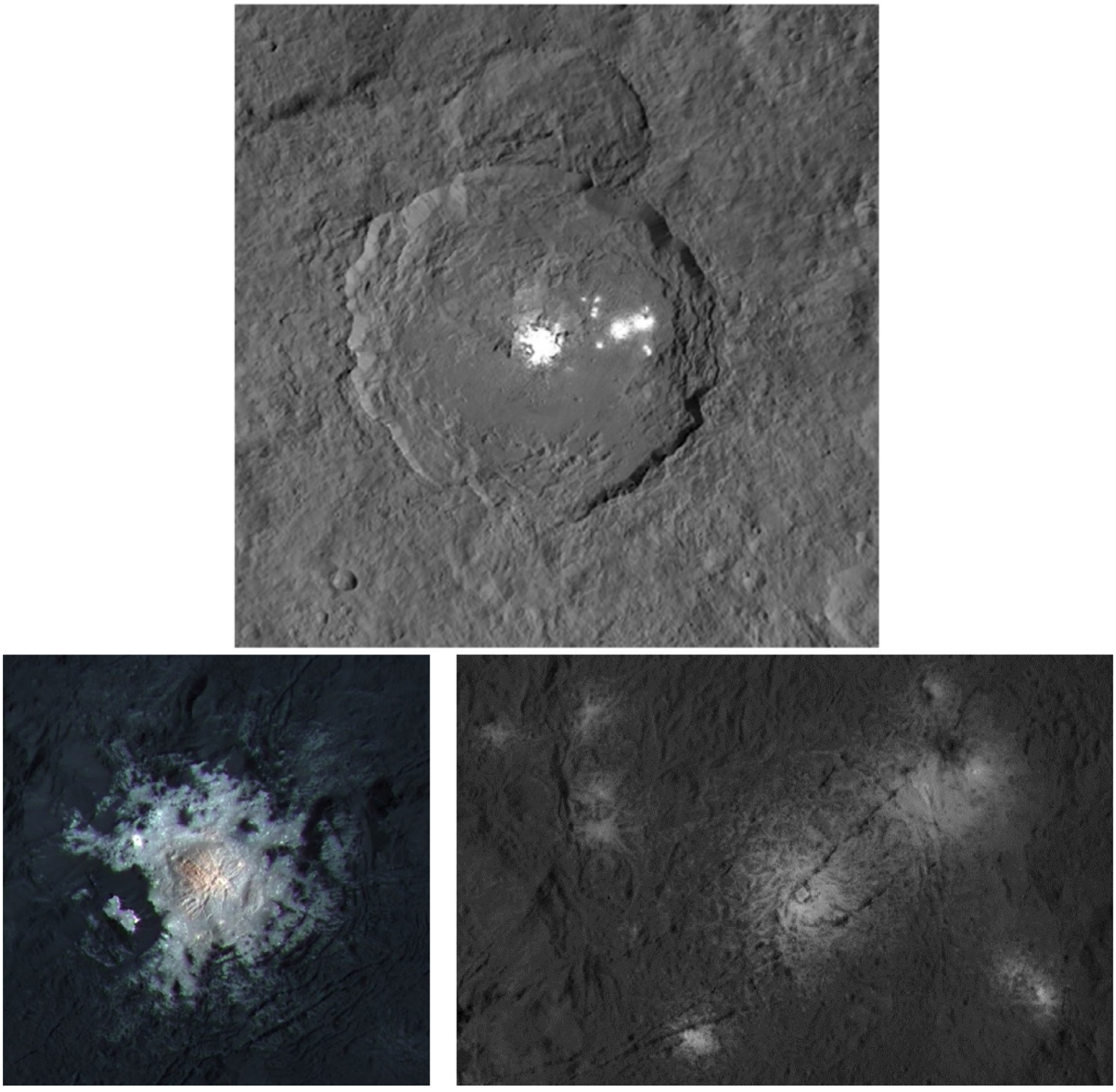

**Fig. 1.** Upper panel. Framing Camera mosaic (35 m/pixel) obtained with clear filter during the Low Altitude Mapping Orbit (LAMO) (Roatsch et al., 2016a,b). Lower left panel: Cerealia Facula obtained by combining framing camera images acquired during LAMO phase with three images using spectral filters centered at 438, 550 and 965 nm, during High Altitude Mapping Orbit (HAMO) phase. Lower right panel: Vinalia Faculae acquired by the framing camera during LAMO phase.

areas, called "Ceralia Facula" and "Vinalia Faculae," in the 92-km-diameter Occator crater (15.8–24.9°N and 234.3–244.7°E). Their albedo is 5–10 times higher than the average surface (Longobardo et al., 2018; Li et al., 2016; Ciarniello et al., 2017; Schroder et al. 2017; Longobardo et al., 2017). Bright material in the faculae has many spectral differences with respect to the crater floor. The OH feature in the spectra of these faculae is shifted from 2.72 to 2.76 µm, indicating the possible presence of Al-phyllosilicates. A very complex spectral feature is present at 3.0 – 3.6 µm, with the superposition of a band at 3.1 µm, two absorption bands at 3.2 and 3.28 µm, and the absorption bands of carbonate at 3.4 and 3.5 µm. The origin of the absorption bands at 3.1, 3.2 and 3.28 µm is still unknown. Moreover, a clear and deep absorption at 4 µm indicates the presence of Na-carbonates (De Sanctis et al., 2016).

Occator crater (Fig. 1) consists of different geological units: smooth and knobby lobate materials, hummocky crater floor material, and the faculae (sorted from the older to the more recent), as discussed by Scully et al. (2018). Dawn's Framing Camera has observed the Cerealia Facula at high spatial resolution (35 m/pix), revealing that it is located in a ~9 km wide and ~700 m deep pit. A dome in the center of the pit rises 0.4 km above the surrounding terrain (Nathues et al., 2017). The faculae are associated with fractures in Occator's floor (Buczkowski et al., 2016). The formation process proposed for the faculae includes impact-induced heating and the subsequent upwelling of volatile-rich materials, possibly rising to the surface along impact-induced fractures from a subsurface brine reservoir (DeSanctis et al., 2016; Scully et al., 2018; Stein et al., 2018). It has also been suggested that some of the faculae could have been deposited from post-impact plumes formed through the boiling of subsurface solutions (Zolotov, 2017; Ruesch et al., 2018).

Here, we use data obtained by the VIR instrument in order to study the mineralogical composition of the Occator crater region. First the data have been thermally corrected, as described in Section 3. Then we analyze the absolute signal levels, spectral slopes, and the spectral parameters of the main absorption bands, as described in Section 4. We also retrieve the abundances and grain sizes of the main minerals identified as components of the

Occator surface materials from a quantitative analysis by means of a radiative transfer model. The model and resulting maps are discussed in Section 5. The overall results and implications are discussed in Section 6 in the general context of the Occator crater evolution.

## 2. Data analysis description

The present work is based on the dataset acquired by the VIR-IR mapping spectrometer. Images provided by the Dawn Framing Camera are also used for context and morphological analysis.

VIR is an imaging spectrometer operating in two channels: the visible channel, ranging between 0.25 and 1.05 µm, and the infrared channel, between 1.0 and 5.1 µm. VIR is capable of high spatial (IFOV = 250 $\mu$rad/pixel, FOV = 64 × 64 mrad) and spectral ($\Delta\lambda$VIS = 1.8 nm/band; $\Delta\lambda$IR = 9.8 nm/band) resolution performance, allowing for the identification of spectral features in order to derive the composition and structure of the surface and its thermal emission.

VIR acquired data of Ceres during all of the mission phases: Survey (spacecraft altitude 4350 km), High Altitude Mapping Orbit (HAMO) (spacecraft altitude 1450 km) and Low Altitude Mapping Orbit (LAMO) (spacecraft altitude 370 km) (Russell and Raymond, 2011). Here we used HAMO and LAMO datasets with nominal spatial resolutions of 400 m/pix and 100 m/pix, respectively.

The calibrated data (Filacchione and Ammannito, 2014) are cleaned of artifacts with the procedure described in Carrozzo et al. (2016). In order to analyze the spectral signature in the range of wavelengths affected by thermal emission, usually from 3.2 µm longward, we remove thermal emission using the method described in Section 3. Photometric effects are corrected for both topographic variations and physical/optical characteristics of the regolith using the Hapke approach (Ciarniello et al., 2017).

We selected all spectra whose footprint is located within ~70 km from the crater center in order to account for the entire crater floor (radius ~45 km) and the ejecta outside the crater rim. The whole dataset contains ~3•10$^5$ spectra of the IR channel. The present work focuses on the spectral range from 1.1 to 4.2 µm, which accounts for 328 out of 432 spectels of the whole range.

## 3. Thermal emission removal

The observed spectra of Ceres' surface are affected by thermal emissions starting from 3.2 µm and towards longer wavelengths. The radiance of the thermal emission hides the absorption bands and prevents a comparison with laboratory reflectance spectra of analogous materials. We implemented a proper algorithm in order to remove the thermal emission. The total radiance is modeled as the sum of the solar radiance reflected by the surface and the thermal emission of the surface, as follows:

- The model of the solar-reflected radiance is produced by a model of reflectance of the surface, multiplied by the solar irradiance at Ceres' heliocentric distance. To be consistent with the spectral modeling discussed in Section 5, we used the same reflectance model to estimate the reflectance level in the thermal emission range.
- A modeled spectrum of thermal emission is summed up to the spectrum from the previous point in order to fit the total radiance. The thermal emission is modeled by the product of Planck function and effective emissivity $\varepsilon_{eff}$. The effective emissivity is modeled as the product of the directional emissivity $\varepsilon_d$ (Hapke, 2012), and the beaming function $\Lambda$ (Davidsson et al., 2009). The directional emissivity $\varepsilon_d$ is a function of the single scattering albedo (thus, it is function of wavelength), and viewing geometry (see Eq. 3 in Section 5). The beaming function $\Lambda$ accounts for unresolved shadow and the roughness of the surface. Following Davidsson et al. (2009), $\Lambda$ is assumed constant in the investigated spectral range. Temperature of the Planck function, and the beaming function $\Lambda$ are free parameters in the modeling and removal of the thermal emission. See Section 5 for further details.
- Once the thermal emission has been derived, we subtract it from the total measured radiance, and we divide the result by the solar irradiance to obtain the reflectance in the whole range.

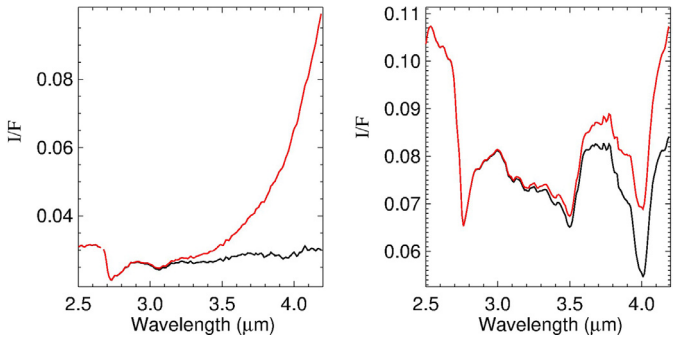


**Fig. 2.** Left panel: thermal emission removal of a typical spectrum of the average surface of Ceres, taken at the rim of the Occator crater. Red and black lines are respectively the I/F spectra before and after thermal emission removal. Right panel: same as left panel for a spectrum acquired at the Vinalia Faculae. (For interpretation of the references to colour in this figure legend, the reader is referred to the web version of this article.)

Examples of the resulting spectra after thermal emission removal are shown in Fig. 2.

The I/F continuum in the thermal emission range, after removal of the emitted radiance, is reflectance model-dependent. In the present work, we consistently use the same reflectance model for all spectra (see Section 5).

## 4. Spectral analysis

### 4.1. Data reduction and methodology

To analyze a large dataset like the one considered in this work, we developed an automatic data process able to retrieve different spectral indicators from Occator crater observations. This algorithm allows for mapping the spatial distribution of spectral properties corresponding to each spectral indicator across the surface. The spectral parameters chosen for this purpose are defined based on the first analysis of the VIR spectra of the average terrain (De Sanctis et al., 2015), and Cerealia and Vinalia Faculae (De Sanctis et al., 2016). The parameters are: photometrically corrected I/F at 2.0 µm, spectral slope between 1.65 and 2.35 µm normalized to the median continuum level in that range, band area and center of phyllosilicate bands at 2.7 and 3.1 µm, band area and center of carbonate bands at 3.5 and 4.0 µm, band area of ammonium salt bands at 2.2 µm, and band area of an unknown component at 3.2 and 3.28 µm mostly present in the faculae.

The band area is defined as:

$$\int_a^b \left[1 - \frac{reflectance(\lambda)}{continuum(\lambda)}\right] d\lambda,$$

where $a$ and $b$ are the edges of the band. The continuum used to characterize the bands is calculated with a linear fit between $a$ and $b$. The band area is expressed in µm units.

The band center is defined as the wavelength corresponding to the minimum of the absorption band after continuum removal.

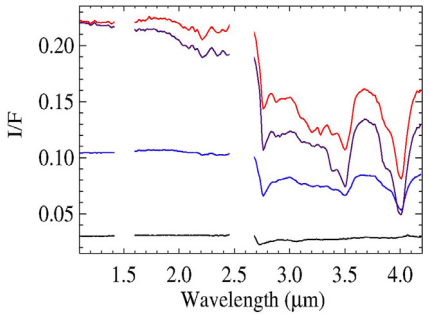


**Fig. 3.** Typical floor spectrum (black line), a Vinalia Facula spectrum (blue line), and two types of Cerealia Facula spectra (red and purple spectrum), which differ in the spectral range 3.2 – 3.4 μm. (For interpretation of the references to colour in this figure legend, the reader is referred to the web version of this article.)

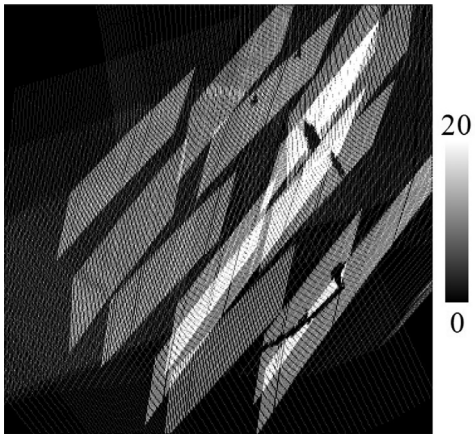


**Fig. 5.** Redundancy map of the matrix which covers the Occator crater region.

The main spectral differences between the average floor of the crater and the faculae are reported in Figs. 3 and 4. The absorption band ascribed to ammoniated salts at 2.08, 2.21, 2.34 μm is deeper on Cerealia Facula, and absent from the floor spectrum. The shift of the band center from 2.72 to 2.76 μm between floor and bright material is ascribed to a change in composition from Mg-phyllosilicates to Al-phyllosilicates. The spectral region at 3.0 – 3.6 μm presents the ammonium phyllosilicates at 3.06 (black spectrum) in the floor spectrum, and the superposition of 3.1, 3.2 and 3.28 μm absorption bands on the bright material. The absorption bands of carbonate at 3.4 and 3.5 μm are deeper in the bright material. The shift from 3.95 μm to 4.01 μm marks the changing composition from Mg–Ca-carbonates to Na-carbonates.

Spectral mapping of the whole crater region was performed by producing a spatial matrix (341 × 341 elements) with a step of 0.05° (~400 m). Taking into account the coordinates of the pixel center of each spectrum, we averaged all derived spectral parameters from pixels with the same spatial coordinates within the step width (Fig. 5 shows the redundancy map). All pixels corresponding to an incidence angle > 70°, emission angle > 70°, or in casted shadow was filtered out to avoid spectral artifacts produced by pixels with low signal-to-noise ratio (S/N). The information on the viewing geometry and illumination was calculated from the shape model and the spacecraft position at the time of the observations.

The maps of each spectral feature are discussed in the next subsections.

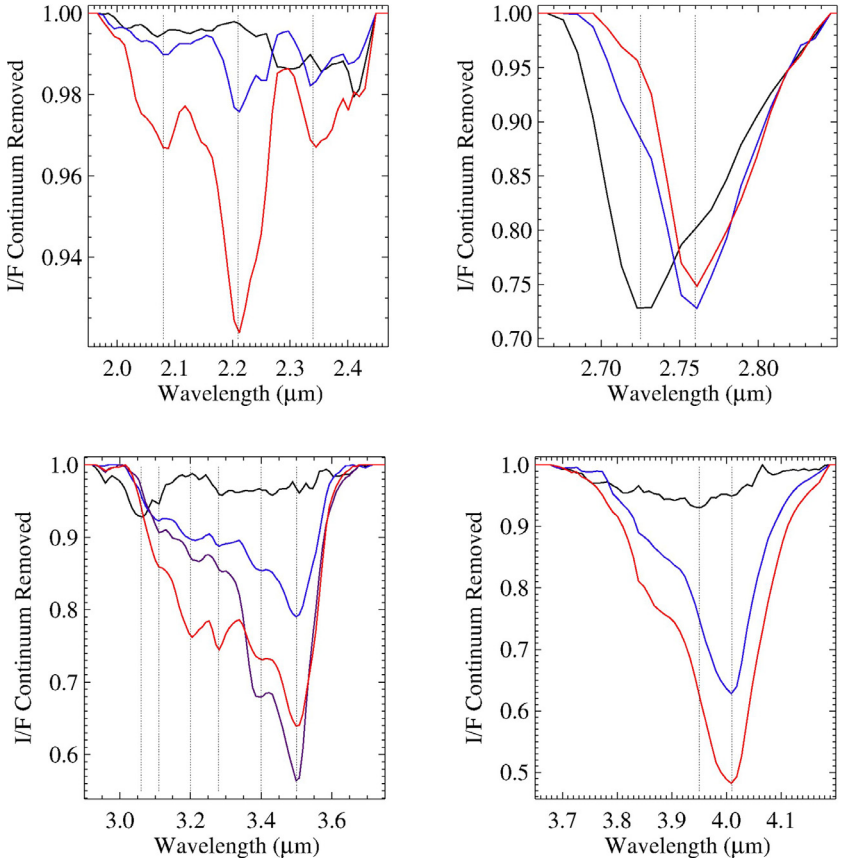


**Fig. 4.** Main spectral difference between a typical floor spectrum (black line), a Vinalia Faculae spectrum (blue line), and Cerealia Facula spectra (red and purple spectra). They are shown after continuum removal. (For interpretation of the references to colour in this figure legend, the reader is referred to the web version of this article.)

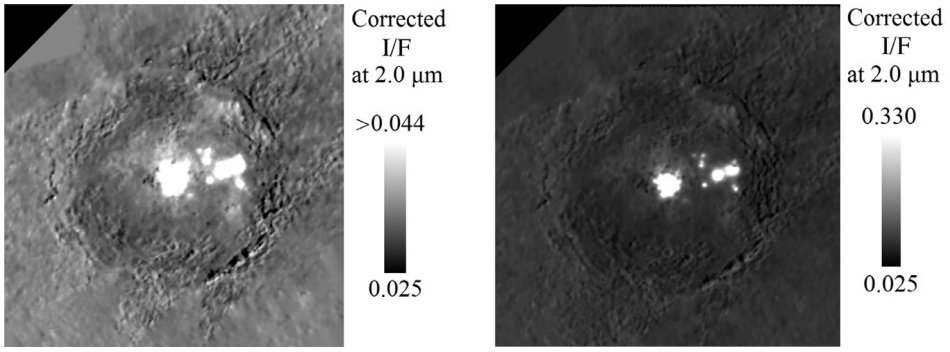


**Fig. 6.** Global maps of photometrically corrected I/F at 2.0 μm (in standard viewing geometry), with different stretching.

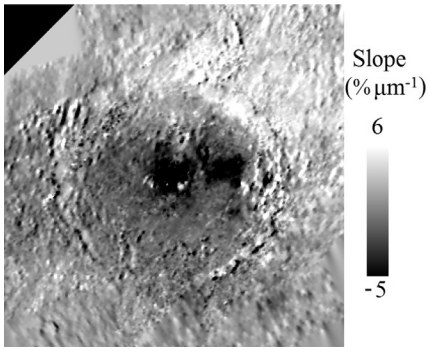


**Fig. 7.** Spectral slope in the range 1.65–2.35 μm.

### 4.2. Global maps

Two maps of photometrically corrected I/F at 2.0 μm with different stretching are shown in Fig. 6 in order to point out all the spatial features of the faculae, the floor, and the ejecta. The corrected maps represent the I/F as seen in standard viewing geometry (incidence angle = 30°, emission angle = 0°), corrected for both for topographic variations and for physical/optical characteristics of the regolith (Ciarniello et al., 2017).

Ceralia Facula, in the center of the crater, is by far the brightest region on the whole Ceres surface. The Vinalia Faculae, composed of two large and several small bright regions, are located in the east part of the floor. Spatial brightness variations can also be detected on the rest of the floor. Brighter areas are located near the faculae and in the north-eastern part of the crater rim. Outside the rim, we can notice different types of ejecta, as already discussed by Longobardo et al. (2017). They are particularly darker in the north-eastern part.

The spectral slope map (Fig. 7) is calculated with a linear fit between 1.65 and 2.35 μm, normalized to the median signal in this spectral range. Different regions can be defined by the spectral slope map: higher values of the slope in the north-eastern ejecta and smaller values corresponding with the faculae. This could be an indication of compositional variations as well as variations in regolith grain size, as yielded by modeling shown in Section 5.

Results for the analysis of the 2.7-μm absorption are shown in Fig. 8. The dichotomy of the ejecta is visible in its band area: larger in the north-eastern part, and smaller in the western part. Variation of the band area can also be seen in all directions outside the rim with a radial pattern. The bright material of Cerealia Facula shows a smaller band area, indicating a lower abundance of phyllosilicates.

The band center is an indicator of composition: the band centered at 2.76 can indicate mainly Al-phyllosilicates (De Sanctis et al., 2016), and the band centered at 2.72 indicates the presence of Mg-phyllosilicates (De Sanctis et al., 2015). The former mostly matches the bright material, whereas the larger abundance of the latter can be observed at the crater rim.

Carbonate absorption bands at 3.5 and 4.0 μm are evident once the thermal emission has been removed. Analysis of their band areas reveals a very good correlation with the brightness of the surface material (see Fig. 9), with the larger values at the faculae, as already discussed in De Sanctis et al. (2016) (see Fig. 10). A good correlation is derived between the band center and the band areas of carbonate absorption bands (right panel of Fig. 10), revealing compositional differences between the faculae (mostly Na-carbonates) and the average material (mostly Mg-carbonates). As in the case of the 2.7-absorption band, relatively larger values of the band area are present at the crater rim.

The spectral parameters of the 3.1 μm absorption band also reveal a dichotomy in the composition of the ejecta (see Fig. 11), with larger band area values in the north-eastern part. The scatter

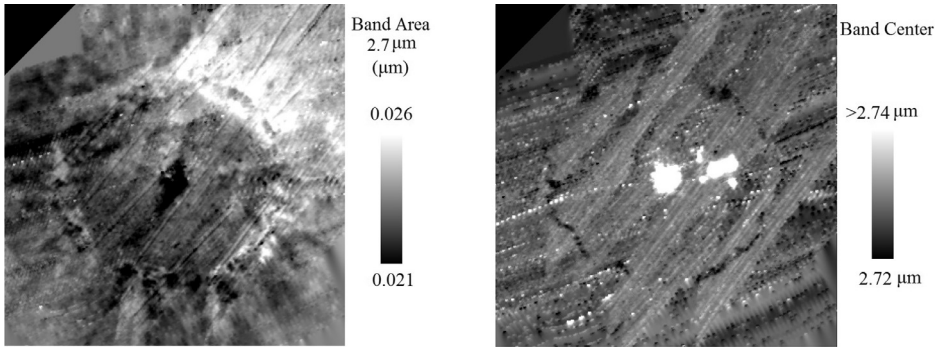


**Fig. 8.** Absorption band at 2.7 μm: band area in the left panel and band center in the right panel. Some stripes are present in the maps as a result of non-filtered artifacts in the spectra.

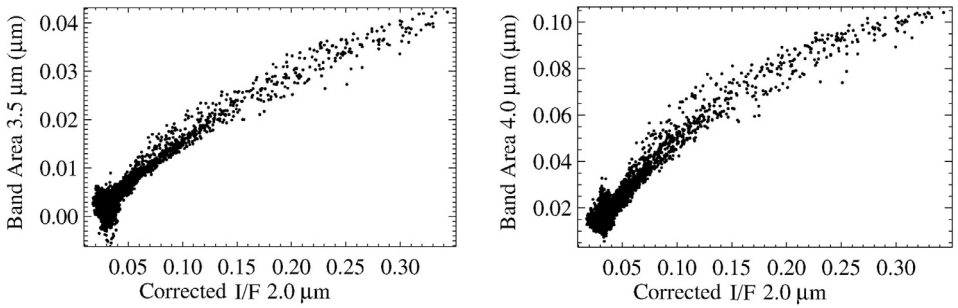


**Fig. 9.** Scatter plot of the carbonate band areas at 3.5 µm (left) and 4.0 µm (right), as a function of the photometrically corrected I/F at 2.0 µm. Points with higher band area and corrected I/F are related to the faculae regions.

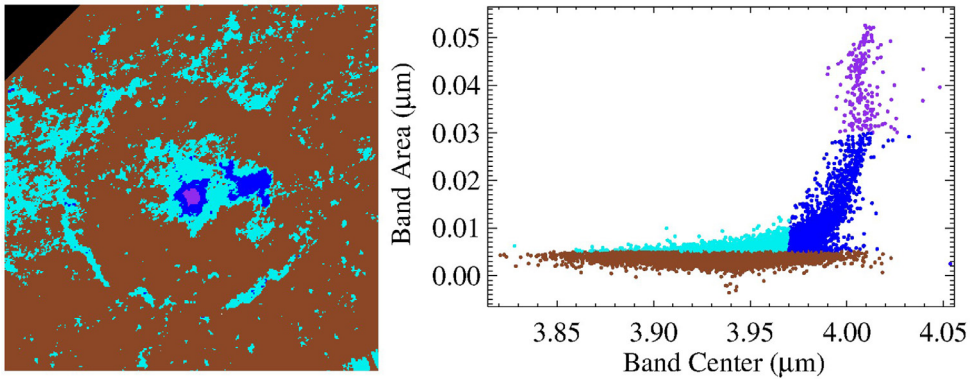


**Fig. 10.** Absorption band center at 4.0 µm as a function of a weighted average of the band areas at 3.5 and 4.0 µm. The colored regions of the map in the left panel match scatterplot colors in the right panel. (For interpretation of the references to colour in this figure legend, the reader is referred to the web version of this article.)

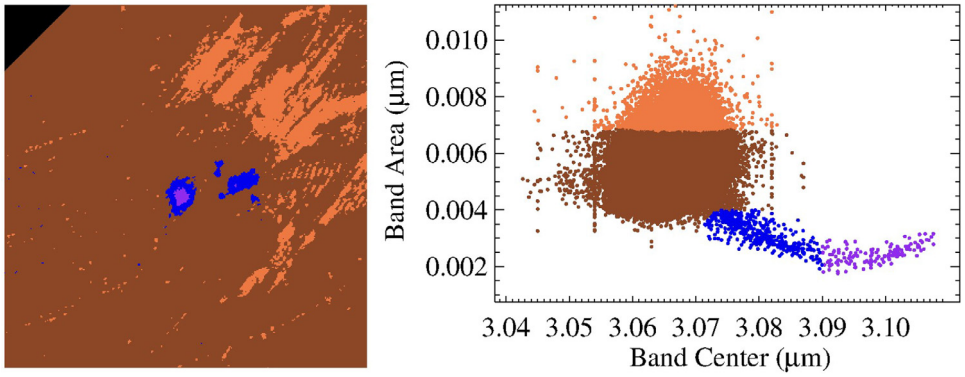


**Fig. 11.** Absorption band center as a function of a band area at 3.1 µm. The colored regions of the map in the left panel match the scatterplot colors in the right panel. Two populations of points can be distinguished on the base of density slice analysis; the upper one is related to the ejecta in the north-eastern part of the map, and the "tail" of the scatterplot is related to the faculae. (For interpretation of the references to colour in this figure legend, the reader is referred to the web version of this article.)

plot depicts a "tail" which is related to the bright material of the faculae: smaller band area values and a shift in the band center. This shift still lacks an explanation in terms of changing composition. It can be related to different components which are partially mixed in the intermediate regions.

### 4.3. Faculae compositional maps

The bright material constituting the faculae is analyzed in detail in this subsection.

Fig. 12 shows a comparison between well-defined spectral parameters of Cerealia Facula: corrected I/F at 2.0 µm, band area at 4.0 µm, band area at 2.2 µm, and band areas of the two shallower absorption bands at 3.2 and 3.28 µm. There is a very good correlation between carbonate band area and corrected I/F. This is an indication that carbonates are the main contributor to the photometric properties of the faculae. Good correlation can also be seen for the other two parameters; however, significant differences can be noted that reflect compositional heterogeneities. The difference in the band area is also a demonstration that the component(s) responsible for the 3.20 and 3.28 µm absorption bands is/are different from the minerals producing the other spectral signatures.

As discussed above, the band center of the phyllosilicates absorption band at 2.7 µm is peculiar in the faculae region, and its analysis can define the edges of the faculae well. Fig. 13 shows that Cerealia Facula has a very jagged edge, different from the very diffuse edges of the Vinalia faculae.

Further analysis of the 3.20 and 3.28 µm absorptions (Fig. 14) shows the sum of their band areas as a function of the corrected I/F at 2.0 µm. The scatter plot reveals that the band areas are correlated to brightness, but with deviations from this trend in specific populations of points: for the same brightness, we have smaller band areas in Vinalia Faculae than in Cerealia Facula, and also significant variations within the Cerealia Facula.

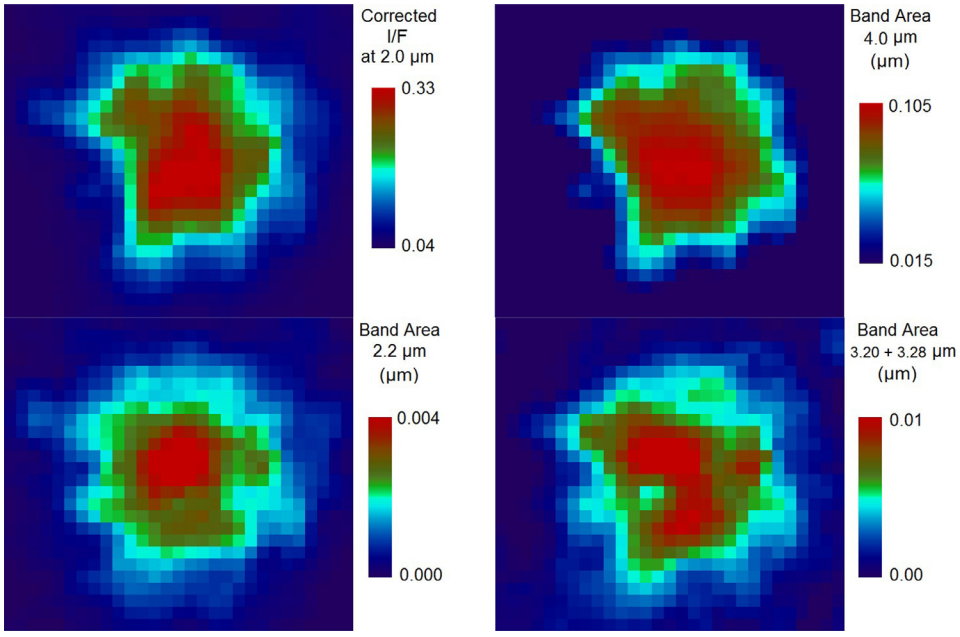


**Fig. 12.** Cerealia Facula maps for different parameters retrieved from the analysis described in Section 4. (For interpretation of the references to colour in this figure legend, the reader is referred to the web version of this article.)

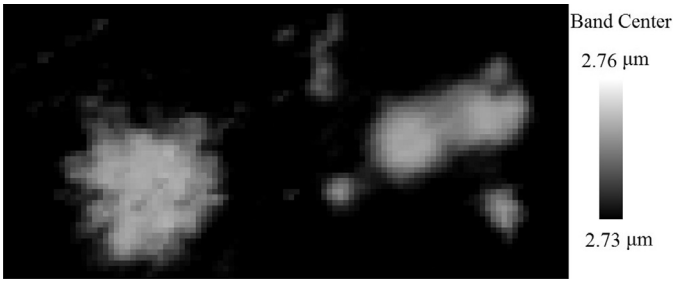


**Fig. 13.** Center of the 2.7 μm absorption band mapped to the faculae.

Similar analysis has been performed for the band area at 2.2 μm (see Fig. 14), which is explained by the presence of ammonium chloride. Also in this case, the scatterplot reveals that the band area is correlated to brightness, but with deviations from this trend in specific populations of points (blue and purple in Fig. 14), which present higher band areas. They are related to a region on the facula that presents a peculiar shape, suggesting a distinct formation event.

## 5. Spectral modeling

To obtain information on the abundances of the minerals making up the surface, we used a quantitative spectral analysis of the composition using Hapke's radiative transfer model (Hapke 1993, 2012). Similar modeling has been described by Ciarniello et al. (2011) and Raponi et al. (2016). The whole formulation of the bidirectional reflectance ($r$) is:

$$r = \frac{SSA}{4\pi}\frac{\mu_0}{\mu+\mu_0}K[B_{SH}p(g) + H(SSA,\mu/K)H(SSA,\mu_0/K) - 1] \times S(i,e,g,\theta)B_{CB} \quad (1)$$

Where $i$, $e$, $g$ are the incidence, emission, and phase angles, respectively, and $\mu_0$, $\mu$ are the cosines of the incidence and emission angles. These parameters come from the shape model and position of the spacecraft at the time of observation. The parameters that contain most of the spectral information are the single scattering albedo ($SSA$), and the related Ambartsumian–Chandrasekhar functions $H(SSA, \mu/K)$ describing the multiple scattering components.

Other parameters that describe the photometric behavior as a function of the viewing geometry, especially the phase function, are:

- the single particle phase function $p(g)$,
- the shadow hiding opposition effect $B_{SH}(g)$,
- the coherent back-scattering opposition effect $B_{CB}(g)$,
- the shadow function modeling large-scale roughness $S(i, e, g, \theta)$, with $\theta$ being the average surface slope.

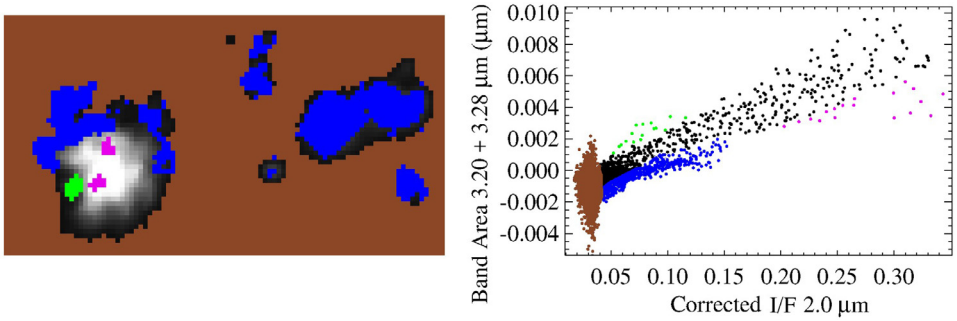


**Fig. 14.** Areas of absorption bands at 3.20 and 3.28 μm as a function of the corrected I/F at 2.0 μm. Different populations of points are divided on the base of their deviation from the general trend and on the base of the density slice analysis. The purple spectrum in Figs. 3 and 4 is representative of the purple regions in the left panel. (For interpretation of the references to colour in this figure legend, the reader is referred to the web version of this article.)

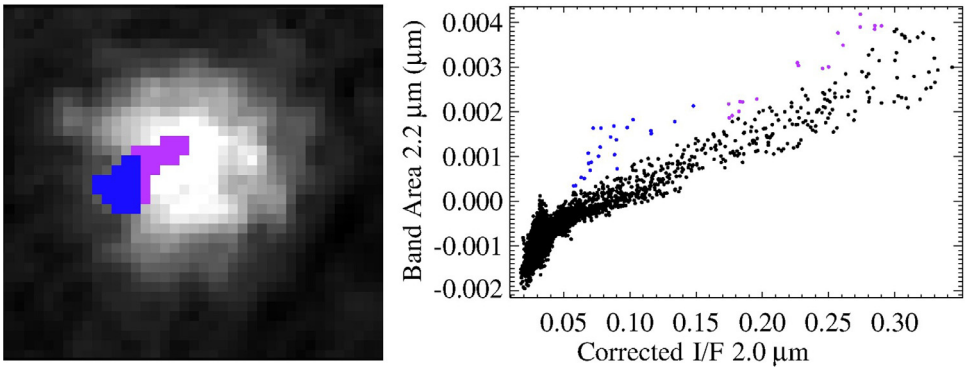


**Fig. 15.** Area of the absorption band at 2.2 µm as a function of the corrected I/F at 2.0 µm. Blue points clearly belong to a distinct population. Here we also highlight the purple region characterized by a broader band area than the average trend, which possibly shares a common origin with the blue region in terms of facula evolution. The blue region is partially overlapped by the green region in Fig. 14. (For interpretation of the references to colour in this figure legend, the reader is referred to the web version of this article.)

**Table 1**
End-members used in calculating optical constants of the mineral types. Spectra are taken from the Relab spectral database.

| Mineral | Type | Sample ID |
|---|---|---|
| Antigorite | Mg-phyllosilicate | AT-TXH-007 |
| Dolomite | Mg–Ca-carbonate | CB-EAC-003 |
| $NH_4$-montmorillonite | $NH_4$-phyllosilicate | JB-JLB-189 |
| Magnetite | Dark material | MG-EAC-002 |
| Heated Natrite | Na-carbonate | CB-EAC-034-C |
| Natrite ($+H_2O$) | Na-carbonate | CB-EAC-034-A |
| Illite | Al-phyllosilicate | IL-EAC-001 |
| Ammonium Chloride | $NH_4$-salt | CL-EAC-049-A |
| Ammonium Bicarbonate | $NH_4$-carbonate | CB-EAC-041-B |

- the porosity parameter $K$, linked to the filling factor (Hapke, 2012).

These photometric parameters are fixed after Ciarniello et al. (2015), who defined the average scattering properties of Ceres' regolith. We assume their values are equal in all types of terrains considered in this work (ejecta, floor, faculae). This assumption is endorsed by the work of Longobardo et al. (2018), which obtained very similar phase functions for the different terrains. The spectral properties are mainly affected by the SSA. The latter have been modeled for an intimate mixing between different minerals, which implies that the particles of the end-member materials are in contact with each other and are all involved in the scattering of a single photon. The SSA of each mineral is defined starting from their grain size and their optical constants, as described in Hapke (2012). The optical constants are derived from laboratory measurements (Table 1) with the method described by Carli et al. (2014).

The average SSA of the regolith is defined through the weight, $p$, which represents the relative abundances of the minerals. The weight $p_i$ is defined as the cross section of the grains of the $i$th mineral as a fraction of the area. $p$ is also a volume fraction, assuming grain sizes are equal for all minerals. Hereafter we refer to the weight $p$ as "abundances."

$$SSA = SSA_{1p1} + SSA_{2p2} + SSA_{3p3} + .. \quad \text{with}: \; p_1 + p_2 + p_3 + .. = 1 \tag{2}$$

The best-fitting result is obtained by comparison of the model with the measured spectra, applying the Levenberg–Marquardt method for non-linear least-squares multiple regression (Marquardt 1963) (see Fig. 16).

Free model parameters to be retrieved are:

(i) Abundances of the end-members and their grain sizes (assumed equal for all end-members);

(ii) A multiplicative constant of the absolute level of reflectance of the model in order to account for uncertainties in the radiometric and photometric accuracies, as well as errors on the local geometry information due to unresolved shadows and roughness;

(iii) A slope added to the model in order to better fit the measured spectrum: in some cases, the measured spectra present an artificial slope where high signal contrast is measured between adjacent pixels, like regions near shadows. This is due to a varying spatial point-spread function towards longer wavelengths (Filacchione, 2006);

(iv) Temperature $T$ and beaming function $\Lambda$ (Davidsson et al., 2009). The latter is free to vary in the range (0–1), and it is multiplied by the directional emissivity $\varepsilon_d$ (Hapke, 2012) to obtain the effective emissivity ($\varepsilon_{eff}$) (see Eq. (3)). The directional emissivity is a function of the SSA (wavelength dependent), and the emission angle. The beaming function accounts for the fact that a macroscopically rough surface does not emit radiation in the same way as a macroscopically flat surface, since there is a variety of local surface normals across the surface (Davidsson et al., 2009). Interpretation of the modeled thermal emission is outside the scope of this work.

$$\varepsilon_{eff} = \wedge \times \varepsilon_d; \quad \varepsilon_d = \sqrt{1 - SSA} \times H(SSA, \mu/K) \tag{3}$$

The total radiance is modeled by accounting for both the contributions of the reflected sunlight, and the thermal emission:

$$Rad = r \times \frac{F_\odot}{D^2} + \varepsilon_{eff} \times B(\lambda, T) \tag{4}$$

where $r$ is the Hapke bidirectional reflectance (Eq. (1)), $F_\odot$ is the solar irradiance at 1 AU, $D$ is the heliocentric distance (in AU), $\varepsilon_{eff}$ is the effective emissivity, $B(\lambda, T)$ is the Planck function. Thus, the estimation of the thermal emission discussed in Section 3 is done simultaneously with the reflectance modeling in order to yield a consistent result between these two contributions to the total signal measured.

The SSA is modeled starting from minerals already discussed in De Sanctis et al. (2015, 2016) (see Table 1), which are related to the average Ceres surface and the composition of the Faculae.

In our previous analysis, this band was assigned to ammonium bicarbonate or ammonium chloride, due to the difficulty in unambiguously determining the carrier. Here, thanks to the high spatial resolution data achieved during the LAMO orbit, the absorption band at 2.2 µm is detected with a high S/N, establishing the role of ammonium chloride in producing this band. Thus, the ammonium bicarbonate, previously considered by De Sanctis et al. (2016), seems unlikely (see Fig. 17) as a possible component

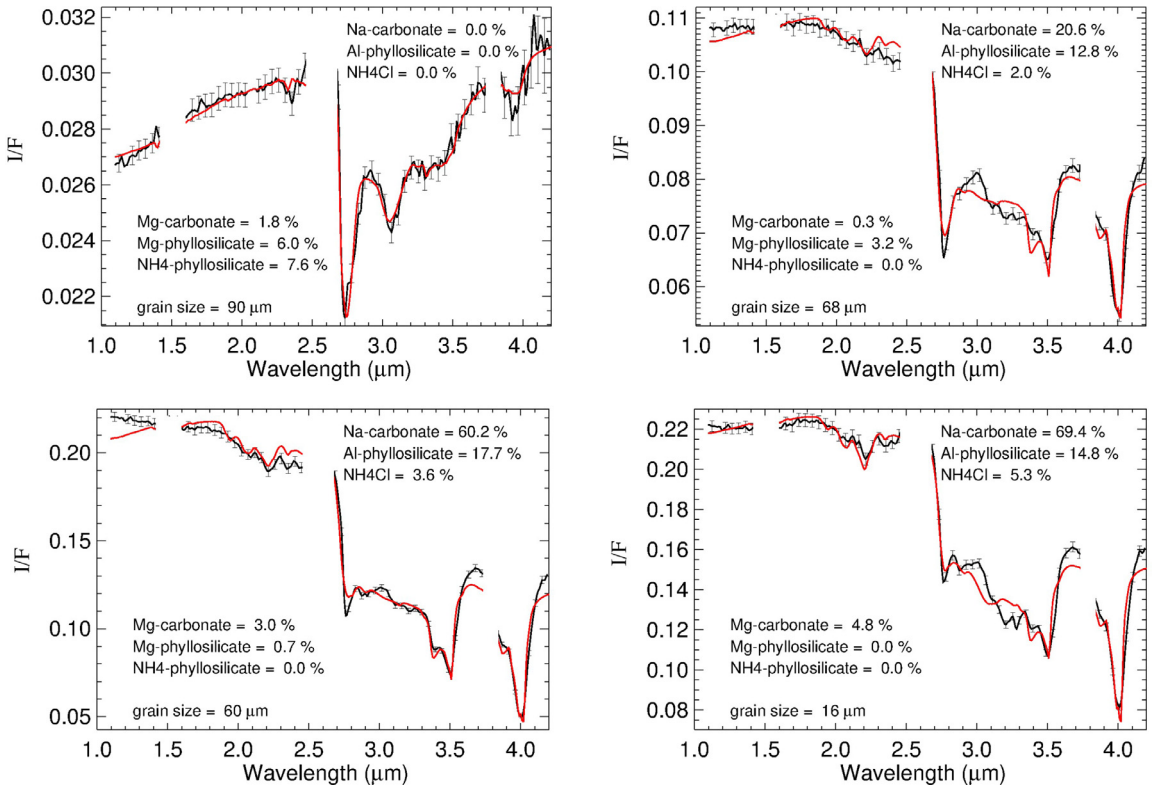


**Fig. 16.** Four examples of best fit measured spectra: crater ejecta (upper left), Vinalia Faculae (upper right), and two spectra of Cerealia Facula. Error bars include poissonian noise and calibration uncertainties.

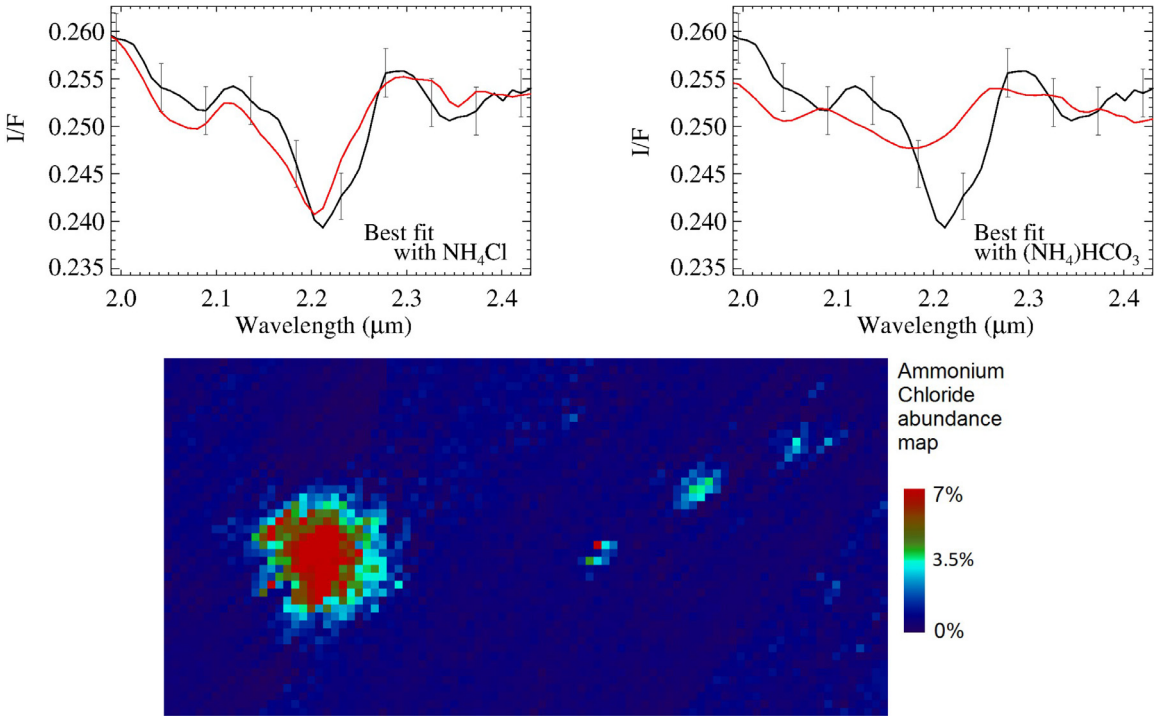


**Fig. 17.** Upper panels: Measured absorption bands at 2.2 µm on Cerealia Facula (black line), and model (red line) performed with ammonium chloride (upper left), and ammonium bicarbonate (upper right). Bottom panel: abundance map of ammonium chloride. The modeling indicates the presence of this mineral on the rest of Occator crater is negligible. (For interpretation of the references to colour in this figure legend, the reader is referred to the web version of this article.)

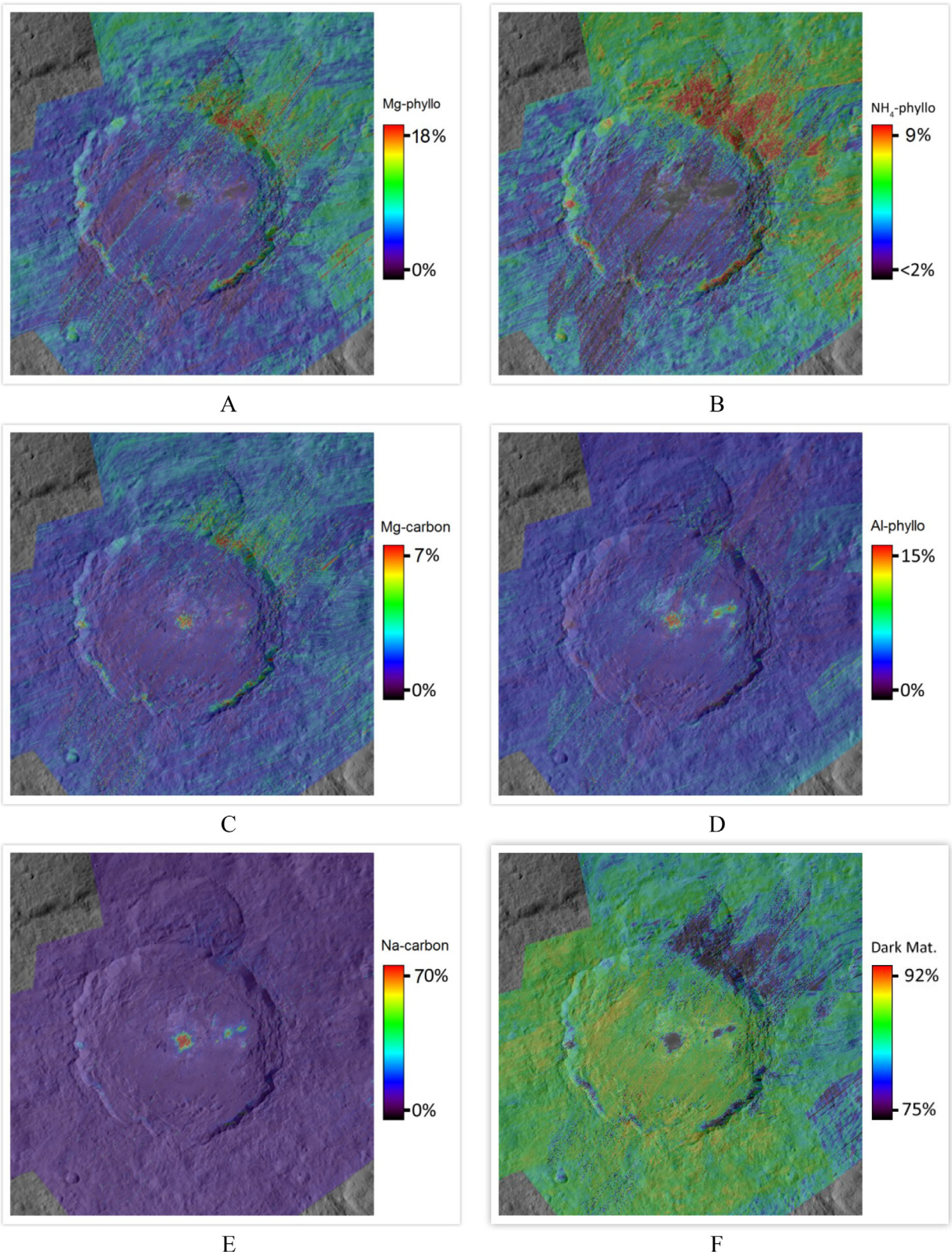


**Fig. 18.** Abundance maps of: A: Mg-phyllosilicate B: $NH_4$-phyllosilicate. C: Mg-carbonate. D: Al-phyllosilicate. E: Na-carbonate. F: Dark material.

of the mixture. However, an amount lower than 1 vol.% of ammonium bicarbonate might be present below the detection limit. The gradient in composition found across Cerealia facula may provide important constraint on the origin of that feature. Indeed, sodium carbonate and ammonium chloride have different eutectic temperatures (~267 K vs. ~247 K, respectively). Hence the enrichment in ammonium chloride toward the center of the facula suggests progressive material extrusion from a cryomagma reservoir whose composition is evolving upon freezing, consistent with the model by Quick (2018).

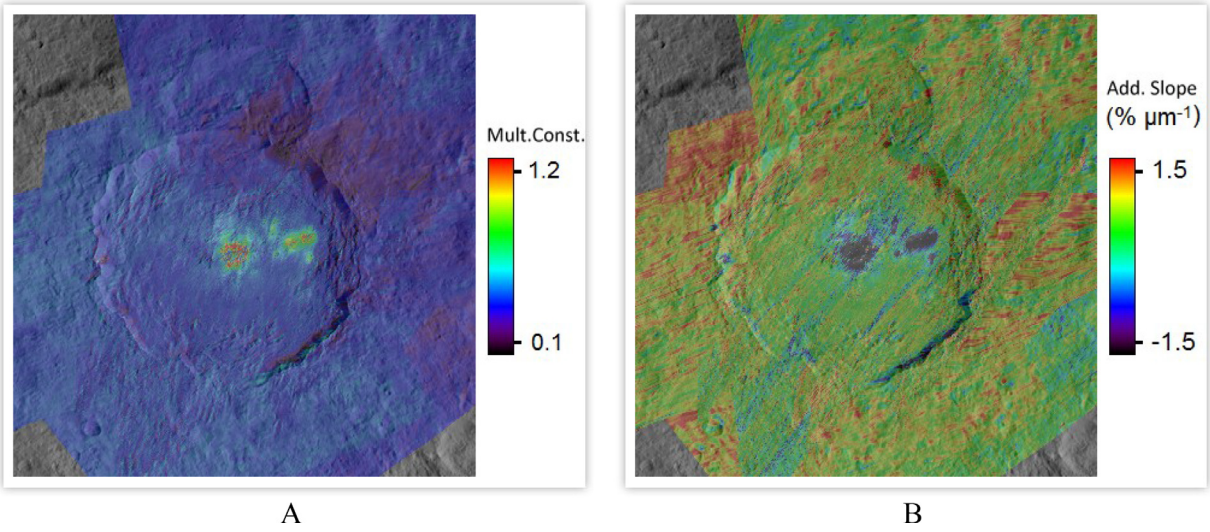


**Fig. 19.** Multiplicative constant (A) and additional slope (B) maps.

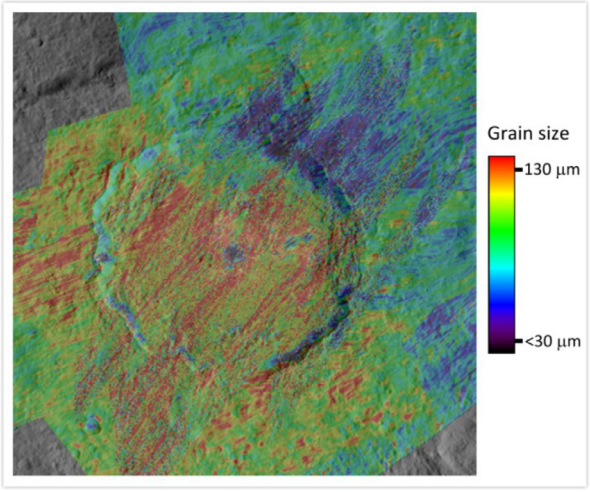


**Fig. 20.** Grain diameter map.

Optical constants of sodium carbonates have been derived from two measured spectra of the same sample under different conditions: hydrated and anhydrous (Carrozzo et al., 2018). When optical constants from both spectra are taken into account, we obtain marginally better fits. However, we cannot establish the presence of hydrated sodium carbonate in the faculae, because the signature of hydration, if present, is shallower than the detection limit.

The maps of abundances (Fig. 18) are superimposed to the Framing Camera mosaic with a transparency of 25% in order to highlight the morphological context.

Sodium carbonate is the most abundant component of the faculae. In the rest of Ceres' surface, the predominant component is a dark material, whose identification is challenging, because its spectrum is featureless, except for the spectral slope. We found a good fit with magnetite ($Fe_3O_4$), however, a large amount of Fe is not consistent with GRaND measurements (Prettyman et al., 2017), hence additional compounds contribute to the dark material. In particular, Ceres' regolith should be composed of a large amount of carbon-bearing material, since carbonaceous chondrite is a close meteoritic analogue (Chapman and Salisbury, 1973; McCord and Gaffey, 1974). Moreover, we emphasize that the model used in this work is based only on spectral features, with the absolute signal level of the model adjusted with the multiplicative constant and the additional slope (Fig. 19).

The grain size map (Fig. 20) shows differences among north-eastern ejecta (30–60 μm), average crater floor (100–130 μm), and material of the faculae (10–60 μm). The average regolith outside the crater has a grain size of ~100 μm. Examples of the retrieval of grains smaller than the average regolith is shown in Figs. 21 and 22, for a spectrum in the north-eastern ejecta and a spectrum of Cerealia Facula, respectively. The best fit is repeated by fixing the

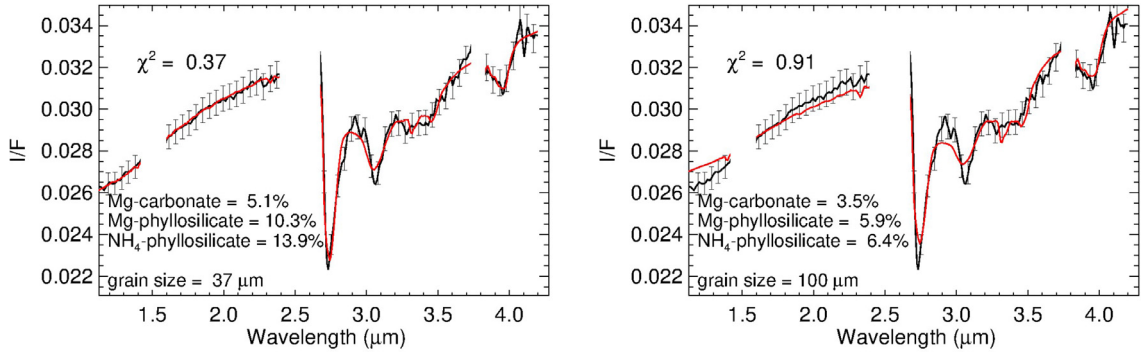


**Fig. 21.** Left panel: best fit of a spectrum of north-eastern ejecta. The retrieved grain size is about 37 μm. Right panel: the best fit is repeated by fixing the grain size to 100 μm, which is the average grain size outside the crater. In the second case, the model does not reproduce the shape of the main absorption bands and the redder slope shortward of 2.5 μm with the same accuracy of the first model.

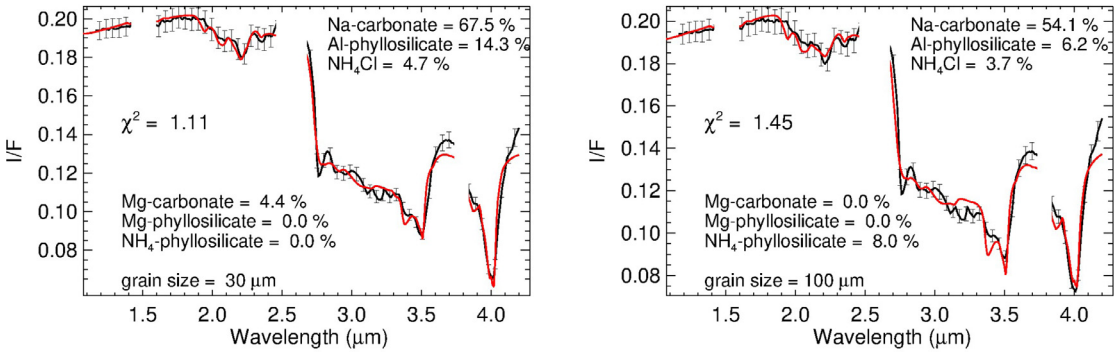


**Fig. 22.** Left panel: best fit of a spectrum in correspondence with Cerealia Facula. The retrieved grain size is 30 μm. Right panel: the best fit is repeated by fixing the grain size to 100 μm. In the second case, the model does not reproduce the shape of the main absorption bands with the same level of accuracy of the first model.

grain size to a larger value (100 μm) but leaving the other parameters free. The resulting models show that the solutions with smaller grains are significantly better.

Not all measured spectra have been well modeled. In particular, the faculae spectra present some features that are still unexplained in term of composition (see Fig. 16), such as the absorption bands at 3.10, 3.20, and 3.28 μm.

## 6. Discussion and conclusions

The region of the Occator crater presents a very diversified mineralogy. Each part of the crater (ejecta, floor, faculae) reveals insights about formation and evolution of the crater. From spectral analysis and spectral modeling, we detect very peculiar ejecta in the north-eastern part of the crater, which shows a larger abundance of all minerals identified on the average surface of Ceres (Mg-phyllosilicates, Mg-Carbonates, $NH_4$-phyllosilicates), and thus a smaller modeled amount of dark material. These detections are apparently in contradiction with the lower albedo of those ejecta. In order to fit the spectra of the ejecta, the model requires a lower multiplicative constant (Fig. 20A). This apparent contradiction can be solved by assuming at least two different types of dark materials: the dark ejecta has a lower concentration of dark material than the rest of the surface, but is dominated by a different type of dark material of much lower albedo. The redder spectra of these dark ejecta are modeled by a small grain size which also point to a different composition.

An alternative explanation for the darker appearance of the ejecta with respect to the average terrain would be a rougher and/or more porous surface; however, both do not explain the different spectral behavior (e.g. the spectral slope as shown in Fig. 7) according to the Hapke model (Eq. (1)).

Similar parameters have been derived for the ejecta and crater walls. This points to a common origin in a reservoir that was lately spread on the surface by the Occator impact event, mostly on the ejecta and partially on the crater walls. Differences in the content of phyllosilicates and carbonates on the global surface of Ceres have already been discussed by Ammannito et al. (2016) and (Carrozzo et al. (2018). These differences could be primordial, or the consequence of heterogeneous upwelling of subsurface material. In both cases, the material has experienced lateral mixing by micrometeoritic impacts. The peculiar ejecta in the north-eastern part of the Occator crater would be an example of this reservoir of material slightly different from the rest of the surface, and preexistent to the Occator crater impact event.

The spectral analysis of the floor near the faculae reveals material that has intermediate properties between bright material and average regolith, pointing to bright material deposition events older than the faculae formation, partially buried by lateral mixing. This is confirmed by the morphological analysis of the crater floor (Scully et al., 2018). The northeastern part of the floor, in which bright material is present, is likely temporally linked to these older deposition events. However, a significant difference with respect to the faculae material is represented by the larger grain size in the entire crater floor. The larger grain size would point to slower cooling conditions, in which larger grains can grow, for example in a melt reservoir. Contrarily, a fast cooling should have taken for the bright material of the faculae. For this reason, the deposition event of floor material could have been very close to the impact event, unlike the more recent faculae formations. However, the different grain size found across the bright material may also be typical of such a complex mineralogy.

The significant depletion of $NH_4$-phyllosilicates and the slight depletion of Mg-phyllosilicates on the floor of the crater are quite common in other Ceres craters (e.g. Ammannito et al., 2016; Longobardo et al., 2017; Raponi et al., 2017), and could be related to the release of $NH_4^+$ and $OH^-$ as a consequence of impact-induced heating.

The specific analysis performed for the faculae has highlighted differences between the Cerealia and Vinalia areas for both mineralogy and morphology. The composition of the Vinalia Faculae presents lower abundances of all components found on Cerealia facula: Na-carbonate, $NH_4Cl$, Al-phyllosilicates, and the unknown component(s) responsible for the bands at 3.20 and 3.28 μm. Moreover, from the map of the band center at 2.7 μm, we also find different shapes for the facula edges: jagged for Cerealia Facula and smooth for Vinalia Faculae.

These differences may have several explanations: (i) different formation mechanisms: subsurface upwelling vs. airborne emplacement (Zolotov, 2017); (ii) different intensities of the formation mechanism (Ruesch et al., 2017); and (iii) different epochs of formation: the lateral mixing from micrometeoritic impacts partially buried the oldest bright material.

Notable differences in the mineralogy are also observed across Cerealia Facula. The mineral distribution does not seem homogeneous, and it is not perfectly correlated to the brightness of the surface, revealing peculiar regions inside the Facula. From the band area map of the ammonium chloride in Cerealia Facula, we identified a region with higher concentration of that mineral than the average trend, whose shape suggests a different emplacement event. Partial superposition between this region and an excess of band areas at 3.20 and 3.28 μm can be also noted.

The overall analysis performed in this work suggests the following evolution for the Occator crater:

- Heterogeneous composition in the deeper layers was preexistent to the impact event in the entire area of the crater. In particular, we can infer the presence of regions with a higher content of phyllosilicates, carbonates, and a reservoir of a ma-

terial darker and redder than the average surface, which produced the north-eastern ejecta;
- The impact event produced a slight depletion of $OH^-$ and $NH_4^+$ in the crater floor, and the melted material on the crater floor favored the growth of larger grains because of the slow cooling;
- The faculae are likely to be formed more recently on the basis of their very different composition, which has not experienced any significant lateral mixing, and on the basis of the smaller grains pointing to faster cooling. Following this argument, Cerealia Facula appears to be more recent than Vinalia Faculae, and/or the emplacing mechanism should be different;
- Different bright material deposition events would have occurred within Cerealia Facula, on the base of its heterogeneous composition that potentially points to an evolution of the composition in the source chamber (e.g., Quick, 2018).

The spectral modeling performed in this work made use of the well-established components of the average surface and faculae materials. We also established the role of the ammonium chloride in producing the absorption band at 2.2 µm. However, some aspects Ceres' faculae composition remain unexplained. In particular, the surface darkening agent is featureless and thus unrecognizable. Moreover, more than one type of dark material should be present based on the above discussion on the nature of the ejecta. We also miss one or several components of the faculae material, which is/are responsible for the absorption bands at 3.11, 3.20 and 3.28 µm. The missing component(s) is/are probably different from the minerals already identified on the faculae, on the basis of the spectral modeling and of the monitoring of band area distributions. Moreover, the need for a multiplicative constant and additional slope, with systematically different values on the faculae with respect to the rest of Ceres' surface, can be explained by the fact that those missing materials alter the signal level in a way that cannot be modeled from the minerals accounted for. Thus, the additional parameters must compensate for them in order to match the signal level.

Further effort in extracting information from the Dawn datasets should be made to complete the mineralogy of Ceres' average surface and the faculae, which could reveal more about the evolution of the dwarf planet.

## Acknowledgments

VIR is funded by the Italian Space Agency-ASI and was developed under the leadership of INAF-Istituto di Astrofisica e Planetologia Spaziali, Rome-Italy. The instrument was built by Selex-Galileo, Florence-Italy. The authors acknowledge the support of the Dawn Science, Instrument, and Operations Teams. This work was supported by ASI-INAF n. I/004/12/0 and NASA.

## Supplementary materials

Supplementary material associated with this article can be found, in the online version, at doi:10.1016/j.icarus.2018.02.001.

## References

Ammannito, E., De Sanctis, M.C., Ciarniello, M., Frigeri, A., Carrozzo, F.G., Combe, J.-Ph., Ehlmann, B.L., Marchi, S., McSween, H.Y., Raponi, A., Toplis, M.J., Tosi, F., Castillo-Rogez, J.C., Capaccioni, F., Capria, M.T., Fonte, S., Giardino, M., Jaumann, R., Longobardo, A., Joy, S.P., Magni, G., McCord, T.B., McFadden, L.A., Palomba, E., Pieters, C.M., Polanskey, C.A., Rayman, M.D., Raymond, C.A., Schenk, P.M., Zambon, F., Russell, C.T., 2016. Distribution of phyllosilicates on the surface of Ceres. Science 353 (6303) id.aaf4279 doi:10.1109/10.1126/science.aaf4279.

Buczkowski, D.L., Schmidt, B.E., Williams, D.A., Mest, S.C., Scully, J.E.C., Ermakov, A.I., Preusker, F., Schenk, P., Otto, K.A., Hiesinger, H., O'Brien, D., Marchi, S., Sizemore, H., Hughson, K., Chilton, H., Bland, M., Byrne, S., Schorghofer, N., Platz, T., Jaumann, R., Roatsch, T., Sykes, M.V., Nathues, A., De Sanctis, M.C., Raymond, C.A., Russell, C.T., 2016. The geomorphology of Ceres. Science 353 id.aaf4332.

Carli, C., Ciarniello, M., Capaccioni, F., Serventi, G., Sgavetti, M., 2014. Spectral variability of plagioclase-mafic mixtures (2): investigation of the optical constant and retrieved mineral abundance dependence on particle size distribution. Icarus 235, 207–219.

Carrozzo, F.G., Raponi, A., De Sanctis, M.C., Ammannito, E., Giardino, M., D'Aversa, E., Fonte, S., Tosi, F., 2016. Artifacts reduction in VIR/Dawn data. Rev. Sci. Instrum. 87 (12) id.124501 doi:10.1063/1.4972256.

Carrozzo, F.G., De Sanctis, M.C., Raponi, A., Ammannito, E., Castillo-Rogez, J.C., Ehlmann, B.L., Marchi, S., Stein, N., Ciarniello, M., Tosi, F., Capaccioni, F., Capria, M.T., Fonte, S., Formisano, M., Frigeri, A., Giardino, M., Longobardo, A., Magni, G., Palomba, E., Zambon, F., Raymond, C.A., Russell, C.T., 2018. Nature, formation and distribution of carbonates on Ceres. Sci. Adv. in press.

Chapman, C.R., Salisbury, J.W., 1973. Comparisons of meteorite and asteroid spectral reflectivities. Icarus 19, 507–522.

Ciarniello, M., Capaccioni, F., Filacchione, G., Clark, R.N., Cruikshank, D.P., Cerroni, P., Coradini, A., Brown, R.H., Buratti, B.J., Tosi, F., Stephan, K., 2011. Hapke modeling of Rhea surface properties through Cassini-VIMS spectra. Icarus 214, 541–555.

Ciarniello, M., De Sanctis, M.C., Ammannito, E., Raponi, A., Longobardo, A., Palomba, E., Carrozzo, F.G., Tosi, F., Li, J.-Y., Schröder, S.E., Zambon, F., Frigeri, A., Fonte, S., Giardino, M., Pieters, C.M., Raymond, C.A., Russell, C.T., 2017. Spectrophotometric properties of dwarf planet Ceres from the VIR spectrometer on board the Dawn mission. Astron. Astrophys. 598 id.A130 doi:10.1051/0004-6361/201629490.

Davidsson, BjörnJ.R., Gutiérrez, PedroJ., Rickman, Hans, 2009. Physical properties of morphological units on Comet 9P/Tempel 1 derived from near-IR Deep Impact spectra. Icarus 201, 335–357.

De Sanctis, M.C., Coradini, A., Ammannito, E., Filacchione, G., Capria, M.T., Fonte, S., Magni, G., Barbis, A., Bini, A., Dami, M., Ficai-Veltroni, I., Preti, G.the VIR Team, 2011. The VIR spectrometer. Space Sci. Rev. 163 (1–4), 329–369. doi:10.1007/s11214-010-9668-5.

De Sanctis, M.C., Ammannito, E., Raponi, A., Marchi, S., McCord, T.B., McSween, H.Y., Capaccioni, F., Capria, M.T., Carrozzo, F.G., Ciarniello, M., Longobardo, A., Tosi, F., Fonte, S., Formisano, M., Frigeri, A., Giardino, M., Magni, G., Palomba, E., Turrini, D., Zambon, F., Combe, J.-Ph., Feldman, W., Jaumann, R., McFadden, L.A., Pieters, C.M., Prettyman, T., Toplis, M., Raymond, C.A., Russell, C.T., 2015. Ammoniated phyllosilicates with a likely outer Solar System origin on (1) Ceres. Nature 528 (7581), 241–244. doi:10.1038/nature16172.

De Sanctis, M.C., Raponi, A., Ammannito, E., Ciarniello, M., Toplis, M.J., McSween, H.Y., Castillo-Rogez, J.C., Ehlmann, B.L., Carrozzo, F.G., Marchi, S., Tosi, F., Zambon, F., Capaccioni, F., Capria, M.T., Fonte, S., Formisano, M., Frigeri, A., Giardino, M., Longobardo, A., Magni, G., Palomba, E., McFadden, L.A., Pieters, C.M., Jaumann, R., Schenk, P., Mugnuolo, R., Raymond, C.A., Russell, C.T., 2016. Bright carbonate deposits as evidence of aqueous alteration on (1) Ceres. Nature 536 (7614), 54–57. doi:10.1038/nature18290.

Filacchione, Gianrico, 2006. Calibrazioni a terra e prestazioni in volo di spettrometri ad immagine nel visibile e nel vicino infrarosso per l'esplorazione planetaria. Università di Napoli Federico II, p. 316.

Filacchione, G., Ammannito, E., 2014. Dawn VIR calibration document. version 2.4. http://sbn.psi.edu/archive/dawn/vir/dwnvvir_i1b/document/vir_calibration/vir_calibration_v2_4.pdf.

Hapke, B., 1993. Theory of Reflectance and Emittance Spectroscopy. Cambridge University Press.

Hapke, B., 2012. Theory of Reflectance and Emittance Spectroscopy. Cambridge University Press, p. 2012.

Konopliv, A.S., Asmar, S.W., Bills, B.G., Mastrodemos, N., Park, R.S., Raymond, C.A., Smith, D.E., Zuber, M.T., 2011. The dawn gravity investigation at Vesta and Ceres. Space Sci. Rev. 163, 461–486.

Li, Jian-Yang, Reddy, Vishnu, Nathues, Andreas, Le Corre, Lucille, Izawa, MatthewR.M., Cloutis, EdwardA., Sykes, MarkV., Carsenty, Uri, Castillo-Rogez, JulieC., Hoffmann, Martin, Jaumann, Ralf, Krohn, Katrin, Mottola, Stefano, Prettyman, ThomasH., Schaefer, Michael, Schenk, Paul, Schröder, StefanE., Williams, DavidA., Smith, DavidE., Zuber, MariaT., Konopliv, AlexanderS., Park, RyanS., Raymond, CarolA., Russell, ChristopherT., 2016. Surface albedo and spectral variability of Ceres. Astrophys. J. Lett. 817, 7 article id. L22.

Longobardo, A., et al., 2017. Mineralogy of the Occator quadrangle. Icarus In press.

Longobardo A., et al. 2018.

McCord, T., Gaffey, M.J., 1974. Asteroids: surface composition from reflectance spectroscopy. Science 186, 352–355.

Marquardt, D., 1963. SIAM J. Appl. Math. 11, 431.

Nathues, A., Platz, T., Thangjam, G., Hoffmann, M., Mengel, K., Cloutis, E.A., Le Corre, L., Reddy, V., Kallisch, J., Crown, D.A., 2017. Evolution of Occator Crater on (1) Ceres. Astron. J. 153, 12 article id. 112.

Palomba E., et al. 2018.

Prettyman, ThomasH., Feldman, WilliamC., McSween, HarryY., Dingler, RobertD., Enemark, DonaldC., Patrick, DouglasE., Storms, StevenA., Hendricks, JohnS., Morgenthaler, JefferyP., Pitman, KarlyM., Reedy, RobertC., 2011. Dawn's Gamma Ray and Neutron Detector. Space Sci. Rev. 163, 371–459.

Prettyman, T.H., Yamashita, N., Toplis, M.J., McSween, H.Y., Schörghofer, N., Marchi, S., Feldman, W.C., Castillo-Rogez, J., Forni, O., Lawrence, D.J., Ammannito, E., Ehlmann, B.L., Sizemore, H.G., Joy, S.P., Polanskey, C.A., Rayman, M.D., Raymond, C.A., Russell, C.T., 2017. Extensive water ice within Ceres' aqueously altered regolith: evidence from nuclear spectroscopy. Science 355, 55–59.

Quick, L., 2018. A possible brine reservoir beneath Occator Crater: thermal and compositional evolution and formation of the Cerealia Dome and Vinalia Faculae. Icarus submitted to (this special issue).

Raponi, A., Ciarniello, M., Capaccioni, F., Filacchione, G., Tosi, F., De Sanctis, M.C., Capria, M.T., Barucci, M.A., Longobardo, A., Palomba, E., Kappel, D., Arnold, G., Mottola, S., Rousseau, B., Rinaldi, G., Erard, S., Bockelee-Morvan, D., Leyrat, C., 2016. The temporal evolution of exposed water ice-rich areas on the surface of 67P/Churyumov–Gerasimenko: spectral analysis. MNRAS 462.

Raponi, A., et al., 2017. Mineralogy of the Coniraya quadrangle. Icarus 2017.

Roatsch, T., Kersten, E., Matz, K.-D., Preusker, F., Scholten, F., Jaumann, R., Raymond, C.A., Russell, C.T., 2016a. Ceres survey atlas derived from Dawn Framing Camera images. Planet. Space Sci. 121, 115–120. doi:10.1016/j.pss.2015.12.005.

Roatsch, T., Kersten, E., Matz, K.-D., Preusker, F., Scholten, F., Jaumann, R., Raymond, C.A., Russell, C.T., 2016b. High-resolution Ceres High Altitude Mapping Orbit atlas derived from Dawn Framing Camera images. Planet. Space Sci. 129, 103–107. doi:10.1016/j.pss.2016.05.011.

Ruesch, O., Nathues, A., Jaumann, R., Quick, L.C., Bland, M.T., Bowling, T.J., Byrne, S., Castillo-Rogez, J.C., Hiesinger, H., Krohn, K., McFadden, L.A., Neesemann, A., Otto, K., Schenk, P., Scully, J., Sykes, M.V., Williams, D.A., Raymond, C.A., Russell, C.T., 2017. Faculae on Ceres: possible formation mechanisms. 48th Lunar and Planetary Science Conference, held 20-24 March 2017, at The Woodlands. Texas LPI Contribution No. 1964, id.2435.

Ruesch, O., et al., 2018. Bright carbonate surfaces on Ceres as remnants of salt-rich water fountains. Icarus submitted to (this special issue).

Russell, C.T., Raymond, C.A., 2011. The Dawn Mission to Vesta and Ceres. Space Sci. Rev. 163, 3–23.

Schröder, S.E., Mottola, S., Carsenty, U., Ciarniello, M., Jaumann, R., Li, J.-Y., Longobardo, A., Palmer, E., Pieters, C., Preusker, F., Raymond, C.A., Russell, C.T., 2017. Resolved spectrophotometric properties of the Ceres surface from Dawn Framing Camera images. Icarus 288, 201–225.

Scully J., et al. 2018.

Sierks, H., Keller, H.U., Jaumann, R., Michalik, H., Behnke, T., Bubenhagen, F., Büttner, I., Carsenty, U., Christensen, U., Enge, R., Fiethe, B., Gutiérrez-Marqués, P., Hartwig, H., Krüger, H., Kühne, W., Maue, T., Mottola, S., Nathues, A., Reiche, K.-U., Richards, M.L., Roatsch, T., Schröder, S.E., Szemerey, I., Tschentscher, M., 2011. The Dawn Framing Camera. Space Sci. Rev. 163 (1–4), 263–327. doi:10.1007/s11214-011-9745-4.

Stein N., et al. 2018.

Zolotov, M.Yu., 2017. Aqueous origins of bright salt deposits on Ceres. Icarus 296, 289–304.